Formation of complex wedding-cake morphologies during homoepitaxial film growth of Ag on Ag(111): atomistic, step-dynamics, and continuum modeling

2009 J. Phys.: Condens. Matter 21 084216

(http://iopscience.iop.org/0953-8984/21/8/084216)

J. Phys.: Condens. Matter **21** (2009) 084216 (12pp) doi:10.1088/0953-8984/21/8/084216

Formation of complex wedding-cake morphologies during homoepitaxial film growth of Ag on Ag(111): atomistic, step-dynamics, and continuum modeling

Maozhi Li[1], Yong Han[2], P A Thiel[3] and J W Evans[4]

[1] Department of Physics, Renmin University of China, Beijing 100872, People's Republic of China
[2] Institute of Physical Research and Technology, Iowa State University, Ames, IA 50011, USA
[3] Departments of Chemistry and Materials Science and Engineering and Ames Laboratory—USDOE, Iowa State University, Ames, IA 50011, USA
[4] Department of Mathematics and Ames Laboratory—USDOE, Iowa State University, Ames, IA 50010, USA

Received 8 July 2008, in final form 29 July 2008
Published 30 January 2009
Online at stacks.iop.org/JPhysCM/21/084216

Abstract
An atomistic lattice-gas model is developed which successfully describes all key features of the complex mounded morphologies which develop during deposition of Ag films on Ag(111) surfaces. We focus on this homoepitaxial thin film growth process below 200 K. The unstable multilayer growth mode derives from the presence of a large Ehrlich–Schwoebel step-edge barrier, for which we characterize both the step-orientation dependence and the magnitude. Step-dynamics modeling is applied to further characterize and elucidate the evolution of the vertical profiles of these wedding-cake-like mounds. Suitable coarse-graining of these step-dynamics equations leads to instructive continuum formulations for mound evolution.

(Some figures in this article are in colour only in the electronic version)

1. Introduction

A central goal of theoretical and simulation studies of epitaxial thin film growth is to develop realistic and predictive models for such processes [1, 2]. A reasonable criterion for success is that such models describe quantitatively all features of the possibly complex multilayer film growth morphologies for a substantial range of deposition conditions (i.e., surface temperature, T, and deposition flux, F). For homoepitaxial growth, a distribution of two-dimensional (2D) islands first forms in the initial submonolayer stage of deposition. Subsequently, mounds (multilayer stacks of 2D islands) develop during unstable multilayer growth in the presence of an Ehrlich–Schwoebel (ES) step-edge barrier [1, 2]. This ES barrier constitutes an additional energetic barrier, above that for intralayer terrace diffusion, which inhibits downward transport [3]. Thus, successful models should describe the lateral size and shape of these islands and mounds, the vertical profile of the mounds, and the evolution of these quantities during growth. To date, examples of models achieving these goals are rare [4, 5].

Deposition of Ag on Ag(111) provides a classic example of rough multilayer growth exhibiting the formation of 'wedding-cake-like' mounds due to the presence of a large ES barrier [5–12]. Here, we develop different types of models for film growth in this system.

(i) *An atomistic lattice-gas (LG) model* [5] for which the key ingredients are: random deposition including downward funneling (DF) at step edges to adsorption sites in lower layers; terrace diffusion leading to nucleation and growth of 2D islands within each layer; dissociation of small sub-stable islands; edge diffusion around the perimeter of larger islands; diffusive downward interlayer transport inhibited by a significant and non-uniform ES barrier.
(ii) *A semi-discrete step-dynamics model* incorporating DF [13] wherein steps at the edge of each atomic layer within a mound are treated as separate continuous curves. These

evolve at a rate determined by the attachment flux to the step. One must also treat the annihilation of steps at valleys between mounds, and the nucleation of new islands (and thus steps) at the peak of mounds [1, 2, 14].

(iii) *A coarse-grained three-dimensional (3D) continuum model* for evolution of a continuous height function describing the vertical profile of an individual wedding-cake versus lateral radius (and an alternative formulation describing radius versus height). Such formulations are most conveniently developed by 'coarse-graining' the step-dynamics model [1, 2, 13–15].

Development of our detailed and realistic atomistic model (i) is guided by close comparison with experimental observations, primarily from scanning tunneling microscopy (STM) studies. Both models of type (ii) and (iii) are instructive for interpreting behavior predicted by the atomistic model and observed in experiment [1, 2]. Often, it will be useful to report lateral positions and distances in terms of the surface lattice constant $a = 0.289$ nm for Ag(111), and vertical heights in terms of the interlayer spacing, $b = \sqrt{2}a/\sqrt{3} = 0.236$ nm.

In section 2, we first present results from Kinetic Monte Carlo (KMC) simulations of our atomistic lattice-gas (LG) model of submonolayer island formation, focusing on transitions in island shape with varying deposition temperature from 120 to 200 K. We also demonstrate that these shapes for higher submonolayer coverages encode information about non-uniformity in the ES barrier. We then present results from KMC simulation of the atomistic LG model for multilayer growth below 200 K. In particular, we assess the magnitude of the ES barrier from an analysis of the size of terraces or islands at the top of mounds. In section 3, we apply step-dynamics modeling which incorporates DF at step edges (assuming a circular island and mound geometry) to provide insight into the vertical mound profiles including the height of the valleys between mounds and the terrace width distribution on the side of the mounds. In section 4, we develop two complementary versions of the continuum evolution equations for mound shape by coarse-graining the step-dynamics equations. Section 5 provides concluding remarks.

2. Atomistic modeling: submonolayer islands and multilayer mounds

We now enumerate in more detail the key ingredients of the atomistic model sketched above in section 1: (i) random deposition of atoms resulting in adsorption at a three-fold-hollow fcc site at the point of impact should one exist, or 'funneling down' to such a site in a lower layer should the atom be deposited at a step edge or on the side of a microprotrusion; (ii) terrace diffusion of isolated adatoms between fcc sites within the same layer with diffusion barrier $E_d = 0.10$ eV established previously [1, 2] and a prefactor $\nu = 10^{11}$ s^{-1} selected to recover the experimentally observed submonolayer island density at lower T; (iii) reversible island formation with critical size $i = 3$, i.e., dimers form reversibly, their dissociation being controlled by a bond energy of $E_b = 0.19$ eV and the above prefactor; larger islands of three or more adatoms are stable (i.e., adatoms cannot detach from them as this typically requires breaking of multiple bonds); (iv) edge diffusion by hopping of adatoms between fcc sites around the perimeter of larger islands; we have used activation barriers for edge diffusion guided by the semi-empirical embedded-atom-method (EAM) and effective-medium theory (EMT) for Ag/Ag(111), but refined to more accurately describe the observed transitions in island shapes (see [16][5] and the following discussion for details); (v) diffusive downward interlayer transport inhibited by a significant and non-uniform ES barrier which will be described in more detail below.

Our model does not include hopping of adatoms to hcp sites or concerted multi-atom hops. Discussion of and support for this simplification is now provided. It is often proposed that diffusion of small clusters (which is excluded from our modeling) can be important during epitaxial growth. Furthermore, it is clear that an accurate description of such small-cluster diffusion in homoepitaxial fcc(111) systems requires incorporation of both occupancy of hcp sites and concerted multi-atom motion [17, 18]. However, since the diffusion barrier for dimers and larger clusters is likely significantly higher than that for monomers, a standard analysis [2] shows that cluster diffusion cannot significantly impact the submonolayer island formation process (or specifically the island density). In addition, it is well known that cluster diffusion does not play a dominant role in post-deposition coarsening of submonolayer island distributions in the Ag/Ag(111) system [20]. For multilayer growth, it has been proposed that cluster diffusion might be important in allowing islands at the top of mounds to migrate so that their edge touches that of the larger supporting island, thereby opening up a fast interlayer diffusion pathway [19]. However, the only observations of such behavior are for much longer timescale post-deposition experiments, and no evidence has been provided that such processes are significant on the much shorter timescale of growth.

Despite these observations, short-range cluster diffusion could have an impact on film growth morphology. This process allows small clusters to at least transiently populate hcp sites. If locked in to such a hcp configuration during growth, this leads to the formation of so-called 'stacking fault islands' (SFI) [21, 22]. SFI have adatoms effectively permanently on hcp sites. This scenario results in the development of anti-phase boundaries between SFI and regular islands (RI) with adatoms on fcc sites which impact subsequent multilayer growth. In some systems, e.g., Ir/Ir(111), the relative population of SFI versus RI can be high [21, 22]. However, our own experimental analysis of SFI for Ag/Ag(111) reveals a negligible population of SFI for the temperatures of interest here [23]. Thus, population of hcp sites and small-cluster diffusion can be safely neglected in the modeling of film growth. See the appendix for further discussion.

We shall see below that concerted exchange does play a role in certain interlayer diffusion processes. However, the final state or atomic configuration is the same for

[5] Edge diffusion barriers were slightly modified from [16] to better describe observed island shapes: 0.28 (0.30 eV) along straight A-(B-)steps; 0.28 (0.33) eV from A-(B-)steps to corners; 0.08 (0.13) eV from corners to A-(B-)steps; the prefactor was 10^{13} s^{-1}.

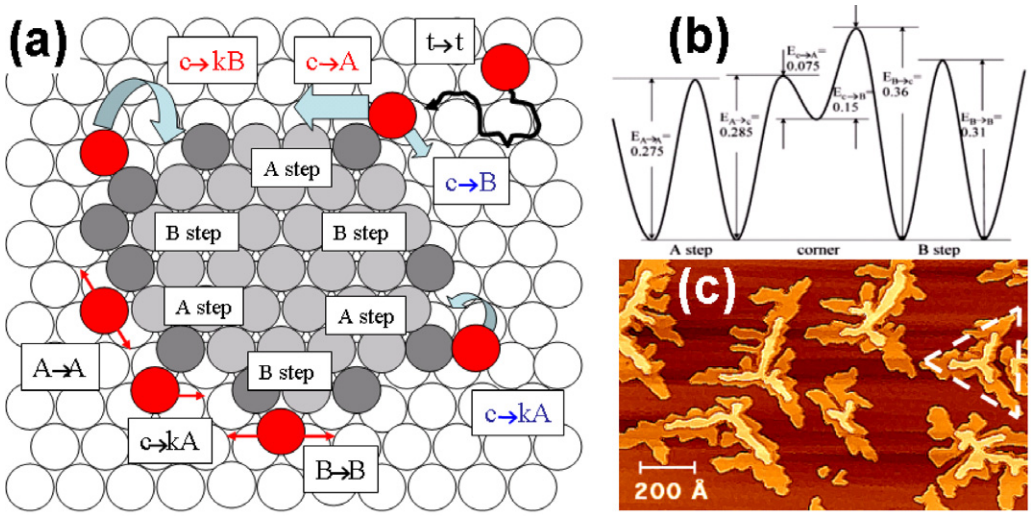

Figure 1. (a) Schematic of edge diffusion processes showing corner diffusion anisotropy (CDA) at corners of hexagonal islands (with atoms directed to A-steps over B-steps), and corresponding enhanced relaxation to step edge of singly-bonded adatoms on B-steps (relative to A-steps). Processes are labeled by the type of step edge (A or B), the type of site (corner, c, or kink, k). (b) PES for edge diffusion around a corner of a hexagonal island [16]. (c) STM image of dendritic islands formed by deposition at 135 K with $F = 0.003$ ML s^{-1}. The lightest color indicates second layer islands. The white dashed lines indicate the orientation of B-steps.

concerted exchange as for standard hopping, so the key factor determining film morphology is the rate rather than the mechanism of interlayer transport. For this reason, we can describe all interlayer diffusion process by hopping but interpret the barrier used to match experimental behavior as corresponding to that for the actual diffusion pathway.

An appealing feature of the Ag/Ag(111) system is that equilibrium island shapes are almost perfect hexagons since the free energies of the (100)-microfaceted A-steps and (111)-microfaceted B-steps in this system are almost equal [20]. This feature is incorporated into our selection of the activation barriers for edge diffusion, which necessarily satisfy detailed balance. Thus, deviations from six-fold symmetry in the lateral growth shapes of islands or mounds (as described below) are purely kinetic in origin. In the experimental and simulation results for film deposition described below at various T, the deposition flux is always selected to be 0.003 ML s^{-1}.

2.1. Submonolayer deposition

In general, restricted edge diffusion in metal(111) homoepitaxial systems, at least at lower T, implies that island shape relaxation is inhibited on the timescale of island growth [1, 2]. This leads to irregular (sometimes fractal or dendritic) island growth shapes. This diffusion-limited-aggregation (DLA) type shape instability is apparent in the simplest DLA hit-and-stick models for aggregation [24]. However, realistic description of island shapes in metal(111) homoepitaxy requires several additional refinements (as are incorporated into our model).

(i) Even at very low T, adatoms which are singly-bonded to another atom at the edge of an island can readily relax to reach more highly coordinated sites at the island edge [25]. Thus, even low T around 100 K, island structure is more dense than in simple DLA models.

(ii) Diffusion along close-packed step edges is quite significant for T above ∼140 K. A consequence is that fractal islands form with 'fat' arms. In the absence of a significant additional kink rounding barrier, as is typically the case in metal(111) homoepitaxy [1, 19], the width of these arms scales like the square root of the edge hop rate [26].

(iii) Metal(111) homoepitaxial systems typically exhibit 'corner diffusion anisotropy' (CDA) wherein singly-bonded adatoms aggregating at the corners of hexagonal islands can more easily reach A-steps than B-steps [16, 25, 27]. CDA also implies that adatoms singly-bonded to other step-edge adatoms, which are either isolated or at the ends of strings of adatoms along sections of close-packed steps, can more easily reach B-steps than A-steps. See figure 1(a) for schematic of these edge diffusion processes, and figure 1(b) for the potential energy surface (PES) describing CDA.

The key aspects of KMC simulation results for island shapes at lower submonolayer coverages for the atomistic lattice-gas model described above are as follows [16].

(a) At lower T around 120–135 K, relaxation to more highly coordinated sites of adatoms aggregating at singly-bonded sites at A-steps (B-steps) is less (more) facile due to CDA. This means that growth orthogonal to A-steps dominates. This produces triangular dendrites with envelopes aligned with B-steps [16]. See figure 1(c) for a STM image showing these islands.

(b) At higher T around 180–200 K, edge diffusion is sufficiently facile to produce compact islands having distorted hexagonal shapes with longer B-steps at low submonolayer coverages, up to $\theta \sim 0.3$ monolayers (ML) [16]. The distortion results from the preference for atoms aggregating at corners where the diffusion flux is

highest to be directed to A-steps due to CDA. This causes A-steps to grow faster resulting in islands with longer B-steps. For higher submonolayer coverages, the details of interlayer diffusion dominate island shape selection producing distinct behavior, as described in detail below.

(c) For intermediate T around 150–160 K, inhibited but active edge diffusion produces roughly isotropic 'fat fractal' islands [16].

For deposition of higher submonolayer coverages, $\theta \sim 0.7$ ML, STM images reveal distorted hexagonal islands with longer A-steps at 180–200 K (rather than longer B-steps which result from CDA at lower coverages) [5][6]. To explain this surprising observation, we note that islands cover most of the substrate at 0.7 ML, so that a correspondingly large fraction of deposited atoms land on top of islands. At these higher T, most of these adatoms can hop down facilitating island growth. With a uniform ES barrier, adatoms would hop down all islands sides with equal probability, so that islands would still have longer B-steps due to CDA. With a non-uniform ES barrier which is lower at B-steps, most atoms would hop down these B-steps causing them to grow faster, thereby resulting in islands with longer A-steps. Thus, the appearance of longer A-steps provides clear evidence for such a non-uniform ES barrier. In section 3, we provide a more detailed description of our treatment of the non-uniform ES barrier [5]. As an aside, such a non-uniformity in ES barrier does not have much influence on the shape of fat fractal islands at around 150 K. Figure 2 compares experimental island shapes with simulation results for both a uniform and a non-uniform ES barrier at 150 and 180 K.

Finally, we comment briefly on the island nucleation process which impacts, e.g., submonolayer island densities. Typically, one introduces a critical size, i, above which islands are stable. At sufficiently low T, island formation will be irreversible ($i = 1$) and the island density will scale like $N_{\rm isl} \sim (F/\nu)^{1/3} \exp[-E_{\rm d}/(kT)]$ [1, 2]. In some metal(111) homoepitaxial systems at low T, $N_{\rm isl}$ is significantly impacted by long-range oscillatory adatom pair interactions, but this is not the case for Ag/Ag(111) [28]. For higher T, one expects a transition to reversible island formation, $i > 1$, first to a reasonably well-defined regime of $i = 2$ (i.e., stable doubly-bonded trimers) [2]. Our '$i = 2$' model described above with a dimer bond strength of $E_{\rm b} \approx 0.19$ eV automatically recovers $i = 1$ behavior significantly below 150 K, but includes some reversibility at 150 K and strong reversibility at 180 K. See section 3. As an aside, this $E_{\rm b}$-estimate came from our density functional theory analysis with a large 6×6 unit cell size [29]. A previous estimate of 0.24 eV, based on a smaller 4×4 cell [28], does not reliably describe the transition to $i > 1$.

2.2. *Multilayer growth*

Multilayer film morphology is controlled by the presence of an ES barrier and to some extent by downward funneling (DF) [1, 2]. Both features are incorporated into our atomistic modeling which also uses the same attempt frequency for inter and intralayer diffusion [5]. In the regime of large ES barrier, $\delta_{\rm ES}$, one expects limited interlayer transport implying Poisson-like growth where root-mean-square film roughness, W, increases like $\theta^{1/2}$ [1, 2]. This type of behavior has been seen in previous diffraction studies of Ag growth on Ag(111) at low T [10–12], and was confirmed in our STM studies [5]. Furthermore, since the ES length, $L_{\rm ES} = \exp[\delta_{\rm ES}/(kT)] - 1$, far exceeds the average submonolayer island separation, $L_{\rm isl} = (N_{\rm isl})^{-1/2}$, each mound is typically built upon a base of a single submonolayer island [1, 2]. One expects prolonged steepening of mound sides during growth, and limited coarsening of their lateral size. The large value of W is not so sensitive to the precise (large) magnitude of $\delta_{\rm ES}$, so other strategies are needed to estimate this important (and much debated [30]) quantity.

Based on the observations of submonolayer islands shapes at 180 K in figures 2(d)–(f), we incorporate a non-uniform ES barrier determined by the local structure of the step edge. We fix the ratio of ES barrier for B- to A-type steps to equal

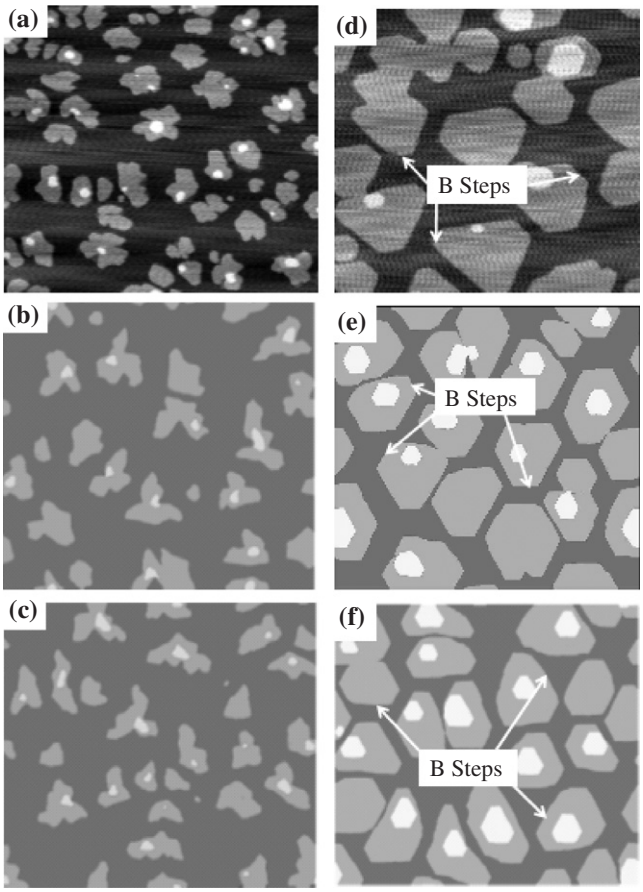

Figure 2. Comparison of STM images ((a), (d)) of islands shapes and predictions of simulations for non-uniform ES barrier ((b), (e)) and uniform ES barrier ((c), (f)) with $F = 0.003$ ML s^{-1}. In the non-uniform case, the barrier at B-steps is half that at A-steps. Fat fractals appear for deposition at 150 K for $\theta \approx 0.3$ ML ((a), (b), (c)). Distorted hexagons appear at 180 K for $\theta \approx 0.7$ ML ((d), (e), (f)) with longer A-steps in (d) and (e), and longer B-steps in (f). Image sizes are 280×280 nm^2. The lightest color indicates second layer islands.

[6] Longer B-steps at high T was incorrectly reported in [16] based on figure 1 in that reference. The sample used at high T is different and oriented at ∼180° from that at low T.

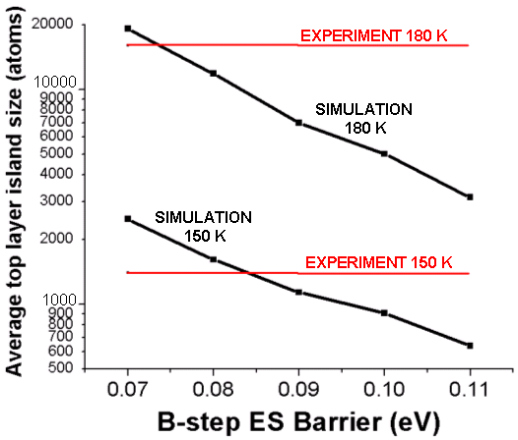

Figure 3. Dependence on the average top layer island size (measured in atoms) on the ES barrier for B-steps, δ_{ES} (B-step), for 3 ML films deposited with flux $F = 0.003$ ML s^{-1}. We set δ_{ES} (B-step) $= 1/2\delta_{ES}$ (A-step). Experimental and simulations results are compared at 150 and 180 K. Estimates for δ_{ES} (B-step) from data at different T are quite consistent (0.085 eV for 150 K, and 0.075 eV for 180 K).

1/2. This choice is guided by and consistent with EAM predictions, which also indicate that exchange provide a facile pathway at B-type but not A-type steps [5]. The magnitude of the ES barrier is determined by exploiting the extreme sensitivity to this quantity of the size of islands or terraces on the tops of mounds (contrasting the behavior of W) [5]. See figure 3. Choosing a value which is too high makes it too difficult for atoms landing on these terraces to hop down. Thus, new higher layers are quickly nucleated by aggregation of these adatoms leading to mounds with small top terraces and anomalously pointed peaks. See figures 4(c), (f) where $\delta_{ES} = \infty$. Instead, choosing δ_{ES} (B-step) ≈ 0.08 eV matches well the experimental top layer island sizes. Compare figures 4(a), (b) (150 K) and 4(d), (e) (180 K).

Note that in order to obtain reasonably *consistent* estimates for δ_{ES} (B-step) from data for the two different temperatures, it is essential to accurately treat the degree of reversibility in island nucleation as this also greatly impacts top layer island size. Using E_b significantly above 0.19 eV, or simply prescribing $i = 1$, produces a large discrepancy: such choices makes island nucleation too easy at higher T forcing a lower choice of δ_{ES} (B-step) at higher T than for lower T.

We have also applied our atomistic model to characterize the evolution of film morphologies for extended growth at 150 K. The lateral shape of the mounds in the first few monolayers of growth is imprinted by the fat fractal shape of the submonolayer islands upon which the mounds are built. However, for thicker films the mounds develop a more geometric shape with a preference for A-facets rather than B-facets. This latter feature, which is shown in figure 5(a) for 20 ML films, was also apparent in earlier diffraction studies which are sensitive to facet structure. Finally, we present results for the vertical film and mound profiles from these simulations for 20 ML films grown at 150 K. Figures 5(b)–(e) show four representative 'line profiles' across the simulation image in figure 5(a). Note that the floor of the valleys between

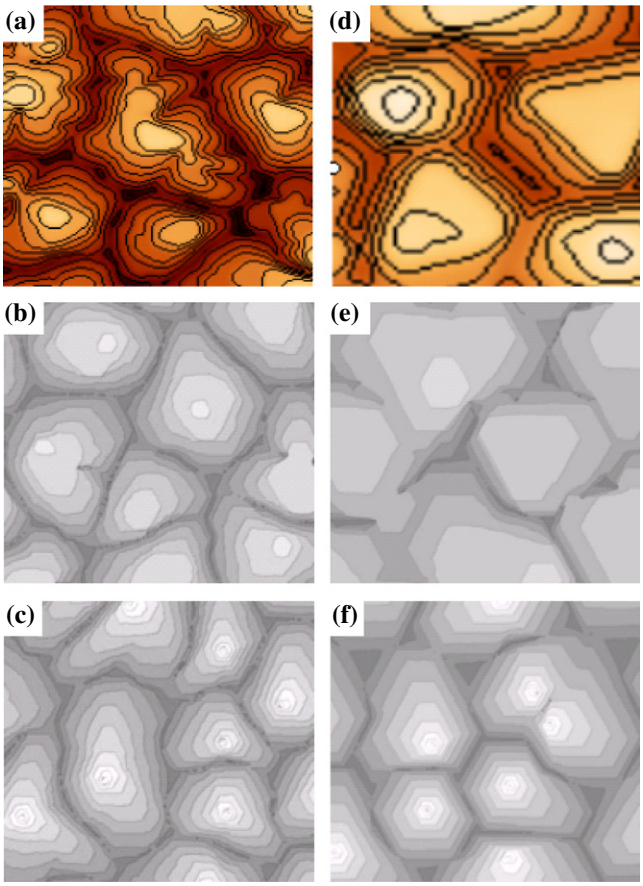

Figure 4. Comparison of experimental ((a), (d)) and simulated morphologies with finite ((b), (e)) and infinite ((c), (f)) ES barrier for 3 ML films deposited with flux $F = 0.003$ ML s^{-1} at 150 K (left row: (a), (b), (c)) and 180 K (right row: (d), (e), (f)). For finite ES barrier we choose δ_{ES}(B-step) ≈ 0.08 eV and δ_{ES} (A-step) $= 2\delta_{ES}$ (B-step). Image sizes are 86×86 nm^2 ((a)–(c)) and 140×140 nm^2 ((d)–(f)).

mounds have a significant height above the original substrate, ranging from 12 to 15 layers for the 20 ML film, and that the valley walls have a finite slope at the base. (The latter is exaggerated in figure 5 due to the different scales for horizontal and vertical directions.) One also observes a distribution of (substantial) sizes for the top layer islands or terraces, where the average of these is similar to the value indicated in figure 3 for 3 ML films grown at 150 K. These various features will be replicated in the step-dynamics modeling including DF presented below in section 3.

3. Step-dynamics modeling: vertical mound profiles

Step-dynamics modeling is particularly effective in providing insight into the shape of the vertical mound profiles and into behavior of related quantities such as the average terrace width [1, 2]. Here, we refine the previous modeling by Krug and co-workers [31, 32] for circular mound geometries to include DF at step edges. This DF process facilitates step annihilation at the valleys between mounds, and thus can greatly impact their vertical profiles.

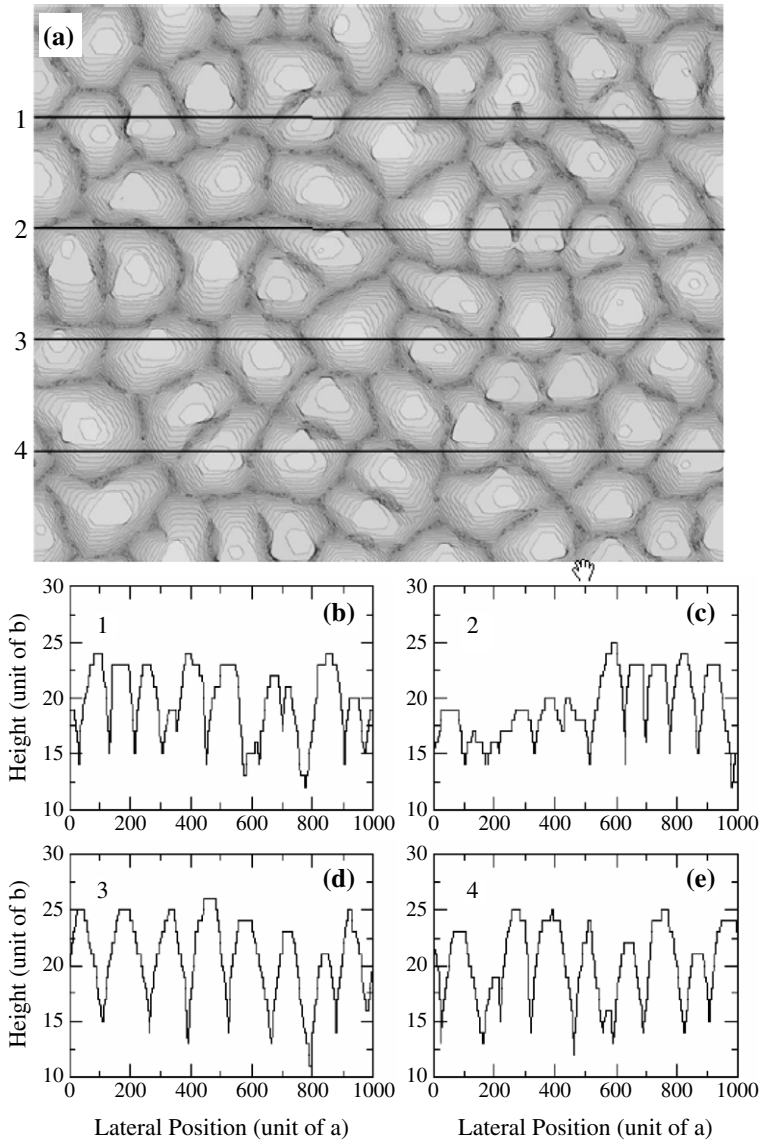

Figure 5. (a) Simulated image (280×280 nm^2) of a 20 ML Ag film deposited on Ag(111) at 150 K with $F = 0.003$ ML s^{-1}. ((b)–(e)) Line profiles across the image at locations indicated in (a). Here 'a' is the (lateral) surface lattice constant and 'b' is the interlayer spacing. Images highlight steps between different layers.

3.1. Theoretical formulation

Our model describes each mound as a set of concentric circular islands, labeled by the number, n, of the layer above the substrate. We let r denote the radial distance from the center of the mound, and let r_n denote the island radii (at locations corresponding to the bottom of the steps). See figure 6. Complete model prescription includes the following ingredients: (a) specifying the growth velocity $v_n = \mathrm{d}r_n/\mathrm{d}t$ for each step; (b) removal of the bottom step, $n = n(\mathrm{min})$, when its radius, $r_{n(\mathrm{min})}$, grows to reach R, the radius of the 'capture zone' of the mound. This removal process corresponds to annihilation with the bottom step in the adjacent mound where this step is traveling in the opposite direction. (c) Nucleation of new islands on top of the mound when the radius, $r_{n(\mathrm{max})}$, of the current top layer island, $n = n(\mathrm{max})$, reaches some critical value $R_c < R$. Below, we comment further on the introduction of new islands with regard to mass conservation.

Thus, at any particular time in this model, the mound is described by $n(\mathrm{max}) - n(\mathrm{min}) + 1$ concentric circular islands labeled by $n(\mathrm{min}) \leqslant n \leqslant n(\mathrm{max})$ with radii satisfying $R_c \leqslant r_{n(\mathrm{max})} < r_{n(\mathrm{max})+1} < \cdots < r_{n(\mathrm{min})} \leqslant R$. This mound should be regarded as sitting on $n(\mathrm{min}) - 1$ complete layers, and the height of the mound measured from valley to peak is given by $\Delta h = [n(\mathrm{max}) - n(\mathrm{min}) + 1]b$, where again b denotes the interlayer spacing.

In prescribing evolution in the step-dynamics model, we regard atoms depositing within the 'step-edge region' a distance c above the descending step n, i.e., for $r_n - c < r < r_n$, as always funneling downward to that step [2, 13]. Atoms landing on the flat (non-step-edge) part of the nth terrace between steps $n + 1$ and n incorporate at the ascending step $n + 1$ with probability P_n^+ and at the descending step n with probability P_n^-. Thus, one has $P_n^+ + P_n^- = 1$. The detailed form of $P_n^\pm$ comes from solving the appropriate boundary

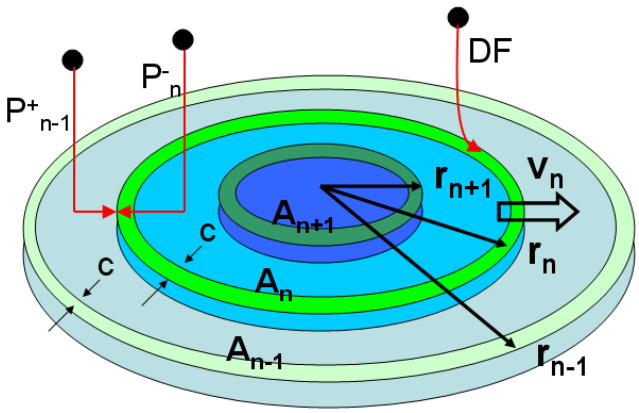

Figure 6. Schematic of circular mound geometry utilized in our step-dynamics modeling including DF.

value problem for the deposition–diffusion equation on this terrace[7]. To incorporate mass conservation, and to facilitate coarse-graining (cf section 4), it is convenient to formulate evolution in terms of island areas, $A_n = \pi r_n^2$. For a 'middle' step with $n(\min) < n < n(\max)$, one has

$$\begin{aligned} \mathrm{d}A_n/\mathrm{d}t &= F[(\sqrt{A_{n-1}} - \sqrt{\pi}c)^2 - A_n]P_{n-1}^+ \\ &\quad + F[(\sqrt{A_n} - \sqrt{\pi}c)^2 - A_{n+1}]P_n^- \\ &\quad + F[A_n - (\sqrt{A_n} - \sqrt{\pi}c)^2] \\ &= F[A_{n-1} - A_n]P_{n-1}^+ + F[A_n - A_{n+1}]P_n^- \\ &\quad - 2\sqrt{\pi}Fc(\sqrt{A_{n-1}}P_{n-1}^+ - \sqrt{A_n}P_n^+) \\ &\quad + \pi Fc^2(P_{n-1}^+ - P_n^+). \end{aligned} \tag{1}$$

This result yields an equation for $v_n = \mathrm{d}r_n/\mathrm{d}t = (2\pi r_n)^{-1}\mathrm{d}A_n/\mathrm{d}t$. Natural refinements are needed for the top step [since it captures all atoms landing on the top terrace for $0 < r_{n(\max)} < R_c$] and for the bottom step [which captures all atoms landing on the lowest terrace for $r_{n(\min)} < r < R$].

The classic model without DF is simply recovered by setting $c = 0$, and all previous analysis was for this case. Most such $c = 0$ analysis set $P_n^+ = 1$ (and $P_n^- = 0$) which produces the feature that the velocity of steps at the bottom of adjacent mounds vanish as the steps approach each other. As a result, steps never annihilate. This classic model ($c = 0$) should provide a reasonable description for Ag/Ag(111) at higher T around 250 K where there is little interlayer transport, and where island and mound sizes are so large that DF plays a limited role (at least in the initial stages of growth up to several dozen ML). The neglect of interlayer transport for Ag/Ag(111) is certainly justified at 150 K and below, but here the effect of DF is more significant as shown below. In particular, for $c > 0$, steps at the bottom of adjacent mounds approach each either and collide with finite velocity at annihilation, even for $P_n^+ = 1$ [2, 13]. For nearly-straight steps with large $r_{n(\min)}$, the specified relative velocity of approach at collision of 2c for $P_n^+ = 1$ is consistent with the behavior of 1D atomistic models[8].

Below all lateral (vertical) distances will be measured in units of surface lattice constant $a = 0.298$ nm (the interlayer spacing $b = 0.236$ nm). R is selected as the average radius for well-developed mounds from STM images, so that $R \approx 70a$ at 150 K. Nucleation of top layer islands is a stochastic process [1, 2]. The critical radius for top layer nucleation, R_c, should thus be regarded as an average radius for top layer nucleation. This quantity should scale like the average radius for top layer islands which is $\sim 20a$ at 150 K. Thus, we choose $R_c = 20a$ at 150 K.

3.2. Numerical results

Results of step-dynamics simulations with $P^+ = 1$ for the evolution of mound profiles are shown in figure 7 for both the classic model with no DF ($c = 0$) and for the refined model including DF ($c = 1/2$). Profiles are shown both for 10, 20, 30, ... ML, and also for a sequence of coverages selected so that the top layer island always has the critical size. The former reveals more effectively the evolution of the top layers, while the latter allows for more systematic assessment of the evolution of the shapes of vertical mound profiles. A key difference between the models is the development of a deep grove at the valley between mounds for the classic model ($c = 0$), also described as the Zeno effect [1]. This behavior reflects the artificial feature that the bottom steps can never annihilate for $c = 0$, so that the valley between mounds remains at the substrate with height zero. In contrast, for $c > 0$, step annihilation does occur, so the mound valley increases in height and the mound slope at the base of the valley remains finite. This behavior was observed in our realistic atomistic simulations in figure 5. In fact, the valley height in those simulations is reasonably consistent with the predictions of the step-dynamics model including DF.

As an aside, we have also performed modeling with variable $P_n^\pm$ choosing parameters appropriate for Ag/Ag(111) at 150 K. In this case, one cannot introduce new top layer islands with zero radius, as the corresponding $P_{n(\max)}^+ = 0$ (see footnote 7). Thus, we introduce mounds with a finite radius of $1/2$. Although this strictly this violates mass conservation, one might just view growth as corresponding to an effective deposition flux slightly above F. (More sophisticated alternatives could be implemented[9]. However, behavior is indistinguishable from that above with $P_+ = 1$.)

Of particular interest in early diffraction studies of Ag/Ag(111) growth at low T [10] was the evolution of the mean terrace width and related quantities. This behavior is readily assessed using our step-dynamics models. Let the

[7] Solution of the steady-state diffusion equation $\partial n/\partial t = F + \nabla^2 n = F + r^{-1}\partial/\partial r(r\partial n/\partial r) \approx 0$ for the adatom density, n, for $r_- < r < r_+$ with boundary conditions $n(r_-) = 0$ (ascending step) and $\partial n(r_+)/\partial r = -n(r_+)/L_{ES}$ (descending step) yields $P_+ = [1/2 - r_+^2(r_+^2 - r_-^2)^{-1}\ln(r_+/r_-)]/[L_{ES}/r_- + \ln(r_+/r_-)]$ where $P_+ + P_- = 1$.

[8] Consider two approaching steps in a 1D atomistic model with $P_+ = 1$, where their approach is due to deposition at sites on the terrace between them together with a contribution due to DF at the steps. Analysis of this finite-state Markov process reveals that the average relative velocity of approach at collision is 2c, consistent with our step-dynamics model.

[9] In a more realistic treatment of top layer nucleation, once the current top island radius reaches the critical value, one does not immediately introduce a new top layer island with finite size. Instead, one waits a finite time until sufficient material has been deposited on top to form a such new top layer island. Top layer island growth is reduced appropriately during this period.

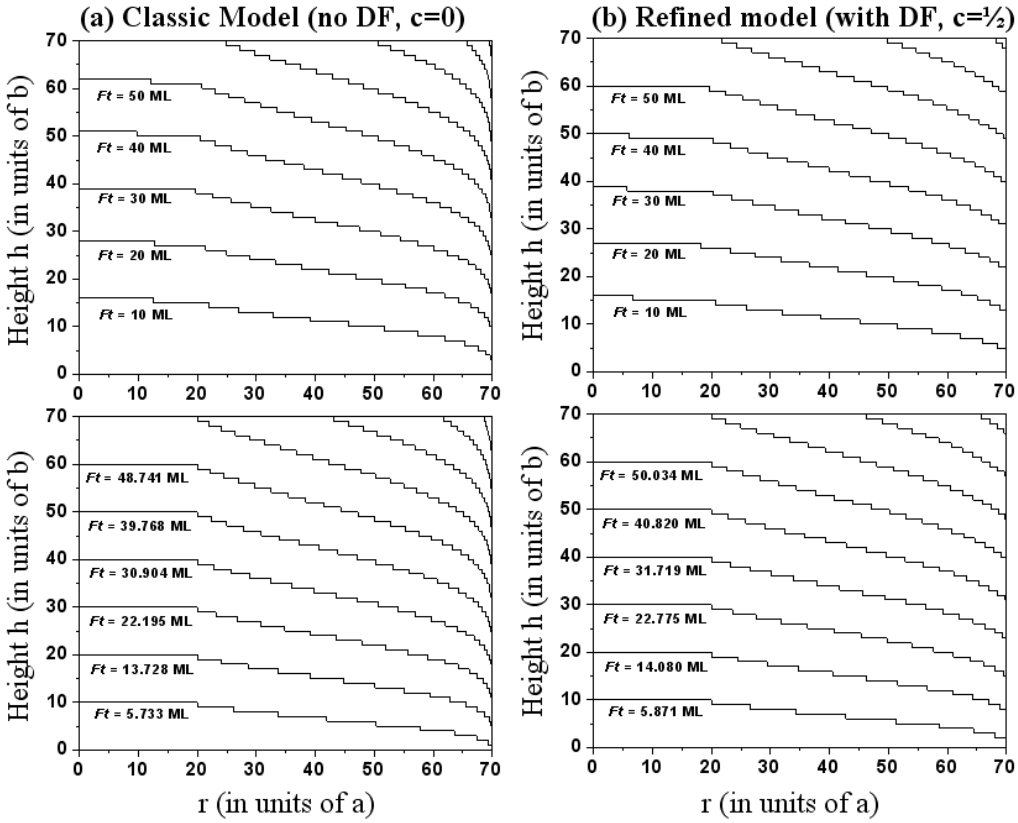

Figure 7. Evolution of vertical mound profiles for $0 < r < R$ from step-dynamics modeling with no interlayer transport ($P_+ = 1$) selecting $R = 70$ and $R_c = 20$: (a) classic model with no DF ($c = 0$); (b) refined model with DF ($c = 1/2$).

width of terrace n be denoted by $L_n = r_n - r_{n+1}$. Then, a standard (std) measure of the average terrace width is $L_{av} = L_{av}(\text{std}) = \sum_n L_n / \sum_n 1$. If the sum includes all terraces, then one has $L_{av}(\text{std}) = R/\Delta h$, where again Δh is the height difference between the valley and peak of the mound. Alternatively, it is natural to restrict consideration to terraces 'on-the-side' of the mound (as done in all results reported below). To this end, we have excluding the special top two terraces since these together constitute the 'top of the mound' with radius typically $\sim R_c$ (cf figures 7(a) and (b)). We also exclude bottom terrace which is typically narrow. Then, for the standard definition of average terrace width, one has that

$$L_{av}(\text{std}) \approx (R - R_c)/\Delta h \tag{2}$$

is still sensitive to Δh and thus to the detailed shape of the valley between mounds. Early studies also considered the variance of the terrace width distribution, $\sigma^2 = \sum_n [L_n - L_{av}(\text{std})]^2 / \sum_n 1$. Finally, it should also be noted that one might naturally consider an area-weighted average terrace width: if $\delta A_n = A_n - A_{n+1}$ denotes the area of terrace n, then this average is given by $L_{av}(\text{area}) = \sum_n \delta A_n L_n / \sum_n \delta A_n$. Figure 8 shows the evolution of both definitions of L_{av} and of σ for the classic model ($c = 0$) and for the model including DF ($c = 1/2$) for terraces on the side of the mound.

Behavior for the classic model ($c = 0$) can be readily understood. The mound height in this model is known to scale like $h(r) \approx \theta + \theta^{1/2} H(r/R)$ where H is a suitable shape function [1, 31, 32]. This scaling together with the identity $h(R) = 0$ implies that $\Delta h \approx \theta + \theta^{1/2} H(R_c/R)$. Consequently, $L_{av}(\text{std})$ should display a rapid asymptotic decrease like θ^{-1}. In contrast, L_{av} (area) should more reflect the Poisson scaling of $W \sim \theta^{1/2}$ and should thus decrease more slowly like $\theta^{-1/2}$. Similarly, it has already been noted that the terrace width in the middle of the mound scales like $\theta^{-1/2}$ [32]. These features are apparent in figure 8(a). For the more realistic model including DF ($c = 1/2$), the behavior of $L_{av}(\text{std})$ is very different, decreasing initially like $\theta^{-1/2}$ and subsequently more slowly. This is reflects a sensitivity to Δh, and specifically to the increase in the height of the valley between mounds for models with $c > 0$. The slow decrease of $L_{av}(\text{std})$ or $L_{av}(\text{area})$ for thicker films also partly reflects the ultimate selection of a well-defined mound shape in this model (in contrast to indefinite steepening in the classic model). As an aside, we note that L_{av} displays significant oscillations when including one or both of the top two terraces. In addition, we have considered the evolution of the standard deviation, σ, of the terrace width distribution. This quantity oscillates significantly for $c > 0$, but decreases with increasing θ for both models.

Finally, we note that this step-dynamics analysis with $c > 0$ (or $c = 0$) does not produce a well-defined $\theta^{-2/3}$ scaling of $L_{av}(\text{std})$ or of σ proposed in diffraction studies of the growth of quite thin Ag/Ag(111) films at low T [10]. We thus expect that this behavior was 'transient or effective scaling' rather than more persistent 'true scaling'.

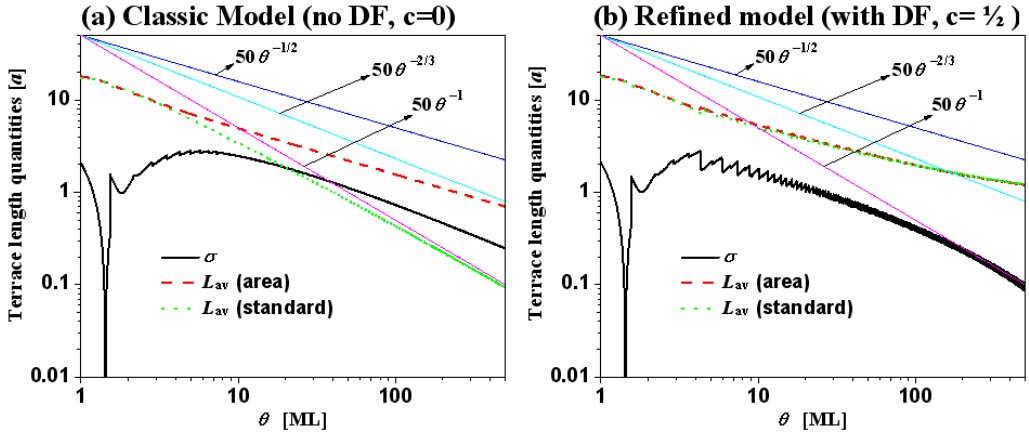

Figure 8. Behavior of the both the standard (standard) and area-weighted (area) average terrace width, $L_{\rm av}$, and well as the standard deviation, σ, of the terrace width distribution for: (a) the classic model with no DF ($c = 0$); (b) the refined model with DF ($c = 1/2$) (for parameters in figure 7). Also shown for comparison are curves corresponding to decay like θ^{-n} with $n = 1, 2/3$, and $1/2$.

4. Coarse-grained 3D continuum modeling

A significant challenge is to derive an evolution equation for a coarse-grained continuum function describing the height, $h(\underline{r}, t)$, of a mound versus lateral position, $\underline{r}$. In our modeling focusing on a single mound with circular symmetry (cf section 3), $h = h(r, t)$ depends only on the radius $r = |\underline{r}|$, and is defined for $0 < r < R$ (where R is the capture zone radius). Also, the mound has a flat top with fixed height $h = h_{\max}(t)$ for $r < R_{\rm c}$ (the critical radius for top layer nucleation). See section 3. To rigorously derive the evolution equation, one might start from either fully-discrete atomistic modeling or from vertically-discrete step-dynamics modeling. Irrespective of the starting point, one anticipates that this evolution equation has the phenomenological form

$$\partial/\partial t\, h(r,t) = Fb - \nabla\cdot\underline{J} = Fb - r^{-1}\partial/\partial r\,[rJ(r,t)],$$
$$\text{where } \underline{J} = J(r,t)\hat{\underline{r}} \tag{3}$$

for $R_{\rm c} < r < R$. Here, $\underline{J}$ denotes the surface diffusion flux, with $\hat{\underline{r}}$ denoting the unit vector in the radial direction. This flux is an intrinsically non-equilibrium quantity proportional to F since detachment from step edges is assumed to be negligible.

Below, we shall set $A_c = \pi R_{\rm c}^2$ and $A_{\max} = \pi R^2$. It is also convenient to consider the mound height measured relative to the average height, $\delta h(r,t) = h(r,t) - Ftb\delta$, so $\partial/\partial t\ \delta h = -\nabla\cdot\underline{J}$. Mass conservation demands that the average mound height satisfies $\langle h\rangle_t = Ftb$ or $\langle\delta h\rangle_t = 0$, i.e., that

$$\int_{0<r<R} {\rm d}r\, 2\pi r\delta h(r,t) = A_c\delta h_{\max}(t)$$
$$+ \int_{Rc<r<R} {\rm d}r\, 2\pi r\delta h(r,t) = 0. \tag{4}$$

From this constraint and using (3), it immediately follows that

$$A_c\,{\rm d}/{\rm d}t\ \delta h_{\max}(t) = -2\pi R_{\rm c}J(R_{\rm c},t) + 2\pi RJ(R,t). \tag{5}$$

Above $\delta h_{\max}(t) = h_{\max}(t) - Ftb$ denotes the height of the top terrace relative to the average height. It is natural to impose the boundary condition $J(R,t) = 0$ simplifying (5).

4.1. Derivation of a traditional evolution equation

To derive an evolution equation of the form (3), one can start with the step-dynamics formulation and imagine fitting a smooth height function, $h(r,t)$, through the top corners of the steps so that $h(r_n,t) = nb$. Then, traditionally [2, 13, 15], one utilizes the fundamental relation

$$\partial/\partial t\, h(r_n,t) = (-{\rm d}r_n/{\rm d}t)\partial/\partial r\, h(r_n,t), \tag{6}$$

and exploits a suitable Taylor expansion about r_n for terms involving $\rm r_{n\pm1}$ in the expression for ${\rm d}r_n/{\rm d}t$ obtained from (1).

However, for the circular geometry considered here, it is more convenient to adopt a different (but equivalent) approach based on a smooth height function $h = h(A,t)$ depending on area $A = \pi r^2$ and starting from the basic relation

$$\partial/\partial t\, h(A_n,t) = (-{\rm d}A_n/{\rm d}t)\partial/\partial A\, h(A_n,t). \tag{7}$$

To express ${\rm d}A_n/{\rm d}t$ in a suitable form starting from (1), we need expansions for $A_{n\pm1}$ about $A_n = A$. Since $h(A_{n\pm1}) - h(A_n) = \pm b = (A_{n\pm1} - A_n)h_A + 1/2(A_{n\pm1} - A_n)^2h_{AA} + \cdots$, it follows that

$$A_{n\pm1} - A_n = \pm(b/h_A) + \tfrac{1}{2}(b^2/h_A)\partial/\partial A(1/h_A)$$
$$\pm (b^3/h_A)\partial/\partial A[(1/h_A)\partial/\partial A(1/h_A)] + \cdots \tag{8}$$

where $h_A = \partial/\partial A\, h(A_n,t)$, etc. Recall that $\delta A_n = A_n - A_{n+1}$ gives the area of terrace n. Then, since (8) implies the relation $h_A \approx -b/\delta A_n$, it follows that $\delta A = b/|h_A|$ provides a measure of terrace area at a specific location in the mound. Below, we provide details of the derivation of a continuum evolution equation only for constant $P_n^{\pm}$. We do not treat the case of variable $P_n^{\pm}$ which is more complicated as these quantities depend on both inner and outer terrace radii.

In the case of the *classic step-dynamics model with no DF* ($c = 0$) and constant $P_n^{\pm}$ (including the case $P_+ = 1$ of most relevance here), the form of the evolution equation (1) for island areas is particularly simple. For $A_c = \pi R_{\rm c}^2 < A < A_{\max} = \pi R^2$, one obtains

$$\partial/\partial t\, h(A,t) = Fb - \partial/\partial A K(A,t), \tag{9}$$

where

$$K(A,t) = \tfrac{1}{2}Fb^2(P^+ - P^-)/h_A - \tfrac{1}{6}Fb^3(1/h_A)\partial/\partial A(1/h_A) + \cdots \text{(no DF, } c = 0). \quad (10)$$

Comparison with (3) suggests the correspondence $K = 2\pi r J$. The first term in K corresponds to the destabilizing uphill current induced by the ES barrier. The second term is associated with up-down symmetry breaking which generally displayed in mound growth shapes, although this term will become relatively insignificant for long times in the model without DF ($c = 0$).

In discussing the general solution of (9), it is more convenient to consider $\delta h(A,t) = h(A,t) - Ftb$ which satisfies equation (5) without the *Fb-term*. Here, we just consider with Zeno-type grooving at the mound valley where one has that $h_A = (2\pi R)^{-1}h_r = \infty$ for $r = R$ or $A = A_{\max}$, so that $K(A_{\max},t) = 0$. In contrast, since $h_A < \infty$ at $r = R_c$, one has that $K(A_c,t) \neq 0$. Then, mass conservation imposes the boundary condition [cf (5)]

$$A_c \mathrm{d}/\mathrm{d}t\, \delta h_{\max}(t) = -K(A_c,t). \quad (11)$$

Finally, we comment on the most important scaling solution consistent with asymptotic Poisson-like growth. For $t \to \infty$, this solution, consistent with (9) and (10), has the form

$$\delta h(A,t) \approx \sqrt{(Ft)}b\varphi(A/A_{\max}), \quad \text{where } \varphi(\alpha) = (P^+ - P^-)\varphi''(\alpha)/\varphi'(\alpha)^2. \quad (12)$$

As indicated above, the first term in K dominates for this solution as $t \to \infty$ and the second is ignored. Its behavior will be elucidated further below in section 4.2. This solution should effectively describe the evolution of larger mounds where DF is not significant, e.g., corresponding to at least initial growth of Ag/Ag(111) at around 250 K.

For the *refined step-dynamics model including DF* ($c = 1/2$) with constant $P_n^{\pm}$ (including $P_+ = 1$), the evolution equation includes the additional terms[10]

$$\partial/\partial t\, h(A,t)|_{\mathrm{DF}} = -2\sqrt{\pi}Fc(\sqrt{A_{n+1}} - \sqrt{A_n})P^+ = Fc\sqrt{(\pi/A)}[-b + \mathrm{O}(b^2)]. \quad (13)$$

These terms do not have the conservative form of (9). However, for the model with $c > 0$, the mound slope is finite at the valley so even $K(A_{\max},t) \neq 0$, and mass conservation must be enforced by an appropriate choice of boundary conditions. The solution of this equation does not have a scaling form like (12), but instead should evolve to the steady-state mound shape. The second term in K above (as well as the first) should impact this shape.

Even analysis of this steady-state solution is non-trivial requiring imposition of appropriate boundary conditions. It is convenient to consider $\Delta h(A,t) = h(A,t) - h(A_{\max},t)$ for which the steady-state equation has the same form as for $h(A,t)$ without the term Fb, i.e., a third-order ODE. We impose the boundary conditions $\Delta h(A_{\max}) = 0$ and $\partial/\partial A\, \Delta h(A_{\max}) = (2\pi R)^{-1}\partial/\partial r\, \Delta h(A_{\max}) = -(2\pi R)^{-1}m_s$ where m_s is the selected slope at the mound valley. Since the steps are quasi-linear near the mound base, to a good approximation m_s should be determined by a 1D analysis which yields $m_s = 1$ for $P^+ = 1$ [2, 13]. Step-dynamics results in section 3 are reasonably consistent with this value. A third boundary condition could be provided by the mound height, $\Delta h = \Delta h(A_c,t) - \Delta h(A_{\max},t)$ measured from valley to the top terrace at $A = A_c$. This quantity is non-trivial, but it is constrained by a flux-balance condition [13].

4.2. Alternative formulation

An alternative strategy for deriving continuum evolution equations is to regard the radius or area of the islands composing the mound as a function of mound height, e.g., consider a continuous function, $A(h,t)$, such that $A_n = A(h_n,t)$. To obtain a corresponding evolution equation utilizing (1), we again need an appropriate expansion for $A_{n\pm1}$ about $A_n = A$. Here, this expansion has the simpler form

$$A_{n\pm1} = A(h_{n\pm1} = h_n \pm b) = A_n \pm b\, A_h + \tfrac{1}{2}b^2A_{hh} \pm \tfrac{1}{6}b^3A_{hhh} + \cdots \quad (14)$$

where $A_h = \partial/\partial h A(h_n)$, etc.

Then, for the *classic step-dynamics model with no DF* ($c = 0$), after replacing A_n by A, etc, substituting the above expansion into the evolution equation (1) for $\mathrm{d}A_n/\mathrm{d}t$ immediately obtains Fokker–Planck-type equation (FPE) for $A(h,t)$. For constant $P^{\pm}$, this FPE has the form[11]

$$\partial/\partial t\, A(h,t) = -Fb\partial/\partial h\, A(h,t) + \tfrac{1}{2}Fb^2(P^+ - P^-)\partial^2/\partial h^2 A(h,t) - \tfrac{1}{6}Fb^3\partial^3/\partial h^3 A(h,t) + \cdots. \quad (15)$$

Changing the independent variable to correspond to a reference frame moving with the growing film, $\delta h = h - Ftb$, removes the first drift term from the FPE for $A(\delta h,t)$. Then, for long-time scaling solutions where the last term in (15) is small (see below), it follows that A satisfies a simple diffusion equation with diffusion coefficient proportional to $(P^+ - P^-)$.

Here, we just consider solutions with Zeno-type grooving at the mound valley so that $A(\delta h,t) \to A_{\max}$ smoothly as $\delta h \to -\infty$. It is necessary to also impose suitable boundary conditions on the evolution equation (15) for $A(\delta h,t)$ at the moving boundary $\delta h = \delta h_{\max}(t)$. In addition to the constraint $A(\delta h_{\max}(t),t) = A_c$, mass conservation requires that

$$A_c \mathrm{d}/\mathrm{d}t\, \delta h_{\max}(t) = -\tfrac{1}{2}Fb^2(P^+ - P^-)A_{\delta h}(\delta h_{\max},t) + \tfrac{1}{6}Fb^3A_{\delta h\delta h}(\delta h_{\max},t) - \cdots, \quad (16)$$

where $\partial B/\partial(\delta h) = B_{\delta h}$, etc, which is entirely consistent with (11). Neglecting the higher-order terms in (15) and (16), as is appropriate for asymptotic scaling solutions (see below), this formulation constitutes a well-posed moving boundary value problem.

[10] These terms have the form $\partial/\partial t\, h|_{\mathrm{DF}} = Fc\sqrt{(\pi/A)}\{-b + b^2[1/2\partial/\partial A(1/h_A) - (4Ah_A)^{-1}] - b^3[(1/6)\partial/\partial A[(1/h_A)\partial/\partial A(1/h_A)] - (4Ah_A)^{-1}\partial/\partial A(1/h_A) + (8A^2h_A^2)^{-1}]\}P_+ + \cdots$

[11] Applying a partial derivative, $\partial/\partial h$, to this equation yields an identical FPE for the local terrace width, $\delta A = \delta A(h,t) = -b\partial/\partial h A(h,t)$ as a function of film height, h. Note that $\int_{h<h\,\max} \mathrm{d}h\delta A(h,t) = (A_{\max} - A_c)b$ should be constant for all t (i.e., normalization of the 'terrace area distribution').

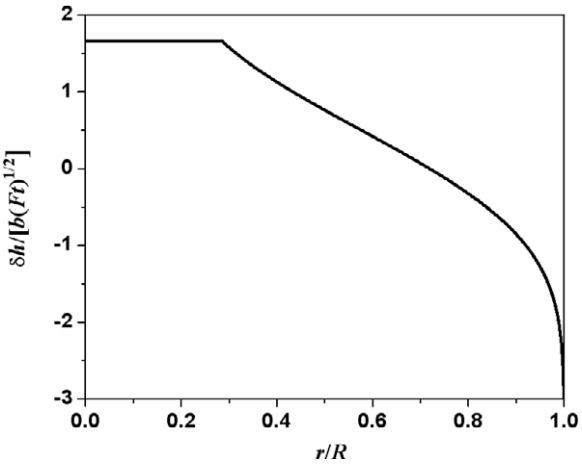

Figure 9. Continuum theory prediction for mound shape in the model without DF ($c = 0$) selecting $R_c/R = 2/7$, consistent with figure 7(a). This analysis follows [32].

Analogous to (7) above, it is natural to look for a scaling solution to (15) consistent with asymptotic Poisson-like growth. These have the form

$$A(h,t) = A_{\max}\Phi[(\delta h = h - Ftb)/(\sqrt{(Ft)}b)],$$
$$\text{where } (P^+ - P^-)\Phi''(z) = -z\Phi'(z). \tag{17}$$

Note that the inflection point of this function always corresponds to the average height or $\delta h = 0$ (cf [32]). The ODE (17) for Φ follows from substitution into (14) ignoring the last small term. It is entirely consistent with the ODE (7) for φ[12], recognizing that φ and Φ are inverse functions, i.e., $\varphi(\Phi(z)) = z$ and $\Phi(\varphi(\alpha)) = \alpha$. The specific form of this scaling solution for Zeno-like grooving at the valley of the mound (where $\Phi(z) \to 1$ as $z \to -\infty$) has been obtained directly for $P_+ = 1$ by Krug and co-workers [32]. For the general case of constant $P_n^{\pm}$, one has that

$$\Phi(z) = 1 - C\{1 + \text{erf}[(P^+ - P^-)^{-1/2}z/\sqrt{2}]\}. \tag{18}$$

Following [32], the height of the top terrace relative to the average height is determined from $\delta h_{\max} = \sqrt{(Ft)}z_{\max}$, where $\Phi(z_{\max}) = A_c/A_{\max}$, and the parameter C is determined by requiring that $\langle z\rangle = \langle \delta h\rangle = 0$.[13] The corresponding mound shape function is plotted in figure 9 for our choice of $A_c/A_{\max} = 4/49$ where $C = 0.4825$ and $z_{\max} = 1.6613$ for $P^+ = 1$. Behavior matches well results of step-dynamics simulations for no DF ($c = 0$) as shown previously [1, 32]. Again, this modeling provides a reasonable description of overall mound shape for Ag/Ag(111) particularly for higher $T \sim 250$ K where DF is not so significant.

For the *refined step-dynamics model including DF* ($c = 1/2$), additional terms appear in the evolution equation beyond those shown in (15). Also, the last term in (15) will be important in determining the steady-state form of the solution. The analysis of this equation is further complicated by the need to impose appropriate boundary conditions at both the valley of the mound and at the top.

[12] If φ satisfies the ODE $G(a, \varphi(a), \varphi'(a), \varphi''(a), ...) = 0$, then it immediately follows that Φ satisfies the ODE $G(\Phi(z), z, 1/\Phi'(z), -\Phi''(z)/\Phi'(z)^3, ...) = 0$.

[13] The latter implies that so that $\int_{0<z<z\,\max} dz\,\Phi(z) = \int_{-\infty<z<0} dz\,\Phi(z)$.

5. Conclusions

A realistic atomistic lattice-gas model has been developed which can successfully provide detailed picture of the complex multilayer mound morphologies which develop during deposition of Ag on Ag(111), particularly for a range of T below 200 K. Step-dynamics modeling provides additional insight into the vertical profiles of mounds developing in this (and in related) systems. In particular, such modeling elucidates the evolution of the average terrace width on the side of mounds. Coarse-grained continuum modeling has the potential to provide further insight into the evolution and selection of mound shapes. A fairly detailed analysis is available for the regime where the effects of DF can be neglected, but challenges remain in developing the theory to treat mound shape selection in the presence of DF.

Acknowledgments

ML was supported by NSF of China (10704088). YH, PAT, and JWE were supported by NSF Grant CHE-0809472, and their work was performed at Ames Laboratory which is operated for the US Department of Energy by Iowa State University under Contract No. DE-AC02-07CH11358.

Appendix. Stacking fault islands (SFI) for submonolayer Ag/Ag(111)

References [21, 22] provide the following picture for SFI island nucleation, which had also been discussed much earlier [33]. Diffusion of small clusters in metal(111) homoepitaxial system in general involves motion between configurations with adatoms on fcc and on hcp sites. It is clear that the larger the cluster, the larger the diffusion barrier for this process, and the larger the energy penalty, $\Delta E > 0$, for the hcp versus the fcc configuration. Thus, for any T, one expects there to be a maximum cluster size, i^*, such that cluster diffusion is significant on the timescale of island growth during deposition. If an atom aggregates with a cluster of size i^*, the growing cluster is thereafter assumed to be frozen in the configuration at the time of aggregation. Thus, the fraction of SFI versus regular islands is roughly given by the population, $\exp[-\Delta E_{i^*}/(k_B T)]$, of hcp relative to fcc configurations of the cluster of size i^*. For Ir/Ir(111), this substantial fraction increases with lower T and exceeds 30% below 300 K [22].

However, our STM analysis of behavior for Ag/Ag(111) reveals far fewer SFI [23]. At 120–135 K, it is easy to distinguish dendritic SFI as they point in the 'wrong direction' relative to regular islands (RI). See figure 10. Interestingly such SFI have the same general shape as RI, a feature supported by EAM studies indicating that the PES for edge diffusion depends only on the nature of the microfaceted step edge (and not whether the island is SFI or RI) [23]. Extensive analysis of such images indicates that the fraction of SFI is only ~4% for deposition at 120–135 K. This fraction should decrease

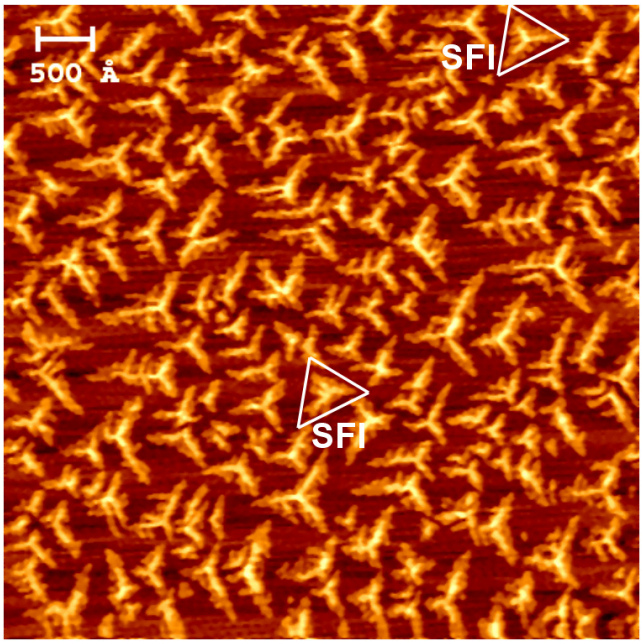

Figure 10. STM image of triangular dendritic islands formed by deposition of 0.4 ML of Ag on Ag(111) at 120 K with $F = 0.004$ ML s^{-1}. Image size is 577 × 577 nm^2. Almost all islands are regular islands (RI) with adatoms of fcc sites, and one arm pointing left. However, examples are provided of two stacking fault islands (SFI) with adatoms on hcp sites, and one arm point right.

for higher T [21, 22]. It is not possible to identify SFI in the regime of fat fractal islands between 150 and 160 K, but observations at higher T of 180–200 K suggest only ∼1% SFI. Thus, our neglect of cluster diffusion and of SFI is well justified, particular at 150 K and above, the regime of most interest here.

References

[1] Michely T and Krug J 2004 *Islands, Mounds, and Atoms* (Berlin: Springer)
[2] Evans J W, Thiel P A and Bartelt M C 2006 *Surf. Sci. Rep.* **61** 1
[3] Schwoebel R L and Shipsey E J 1966 *J. Appl. Phys.* **37** 3682
Ehrlich G and Hudda F G 1966 *J. Chem. Phys.* **44** 1039
[4] Caspersen K J, Layson A R, Stoldt C R, Fournee V, Thiel P A and Evans J W 2002 *Phys. Rev.* B **65** 193407
[5] Li M, Chung P-W, Cox E, Jenks C J, Thiel P A and Evans J W 2008 *Phys. Rev.* B **77** 033402
[6] Meinel K, Klaua M and Bethge H 1988 *J. Cryst. Growth* **89** 447
[7] van der Vegt H A, van Pinxteren H M, Lohmeier M, Vlieg E and Thornton J M C 1992 *Phys. Rev. Lett.* **68** 3335
[8] Vrijmoeth J, van der Vegt H A, Meyer J A, Vlieg E and Behm R J 1994 *Phys. Rev. Lett.* **72** 3843
[9] Ammer Ch, Schaefer T, Teichert Ch, Meinel K and Klaua K 1994 *Surf. Sci.* **307–309** 570
[10] Luo E Z, Wollschlager J, Wegner F and Henzler M 1995 *Appl. Phys.* A **60** 19
[11] Elliot W C, Miceli P F, Tse T and Stephens P W 1996 *Phys. Rev.* B **54** 17934
[12] Wollschlager J, Luo E Z and Henzler M 1998 *Phys. Rev.* B **57** 15541
[13] Li M and Evans J W 2005 *Phys. Rev. Lett.* **95** 256101
Li M and Evans J W 2006 *Phys. Rev. Lett.* **96** 079902E
[14] Politi P and Villain J 1996 *Phys. Rev.* B **54** 5114
[15] Kohn R V, Lo T S and Yip N K 2002 *MRS Proc.* **696** T1.7
[16] Cox E, Li M, Chung P-W, Ghosh C, Rahman T S, Jenks C J, Evans J W and Thiel P A 2005 *Phys. Rev.* B **71** 115414
[17] Chang C M, Wei C M and Chen S P 2000 *Phys. Rev. Lett.* **85** 1044
[18] Karim A, Al-Rawi A N, Kara A, Rahman T S, Trushin O and Ala-Nissila T 2006 *Phys. Rev.* B **73** 165411
[19] Giesen M, Schultze Icking-Konert G and Ibach H 1998 *Phys. Rev. Lett.* **80** 552
[20] Morgenstern K 2005 *Phys. Status Solidi* b **242** 773
[21] Busse C, Polop C, Mueller M, Albe K, Linke U and Michely T 2003 *Phys. Rev. Lett.* **91** 056103
[22] Polop C, Lammerschop A, Busse C and Michely T 2005 *Phys. Rev.* B **71** 125423
[23] Chung P-W, Ghosh C, Li M, Evans J W and Thiel P A, unpublished
[24] Witten T A and Sander L M 1981 *Phys. Rev. Lett.* **47** 1400
[25] Hohage H, Bott M, Morgenstern M, Zhang Z, Michely T and Comsa G 1996 *Phys. Rev. Lett.* **76** 2366
[26] Bartelt M C and Evans J W 1994 *Surf. Sci. Lett.* **314** L829
[27] Brune H, Roder H, Bromann K, Kern K, Jacobsen J, Stoltze P, Jacobsen K and Norskov J 1996 *Surf. Sci.* **349** L115
[28] Fichthorn K and Scheffler M 2000 *Phys. Rev. Lett.* **84** 5371
[29] Shen M, Jenks C J, Thiel P A, Liu D-J and Evans J W 2007 *Phys. Rev.* B **75** 245409
[30] Bromann K, Brune H, Roeder H and Kern K 1995 *Phys. Rev. Lett.* **75** 677
Morgenstern K, Rosenfeld G, Laegsgaard E, Besenbacher F and Comsa G 1998 *Phys. Rev. Lett.* **80** 556
Roos K R and Tringides M C 2000 *Phys. Rev. Lett.* **85** 1480
Roos K R and Tringides M C 2001 *Phys. Rev. Lett.* **87** 149602
Roos K R and Tringides M C 2001 *Phys. Rev. Lett.* **87** 149604
Roos K R and Tringides M C 2001 *Phys. Rev. Lett.* **87** 149606
Krug J 2001 *Phys. Rev. Lett.* **87** 149601
Morgenstern K and Besenbacher F 2001 *Phys. Rev. Lett.* **87** 149603
Heinrichs S and Maass P 2001 *Phys. Rev. Lett.* **87** 149603
Heinrichs S and Maass P 2002 *Phys. Rev.* B **66** 066112
Heinrichs S, Roettler J and Maass P 2000 *Phys. Rev.* B **61** 6057
Roettler J and Maass P 1999 *Phys. Rev. Lett.* **83** 3490
Krug J, Politi P and Michely T 2000 *Phys. Rev.* B **61** 14037
Chvoj Z and Tringides M C 2002 *Phys. Rev.* B **66** 035419
[31] Krug J 1997 *J. Stat. Phys.* **87** 505
[32] Krug J and Kuhn P 2002 *Atomistic Aspects of Epitaxial Growth* (*NATO ASI*) ed M Kotrla *et al* (Dordrecht: Kluwer)
[33] Meinel K, Klaua M and Bethge H 1988 *Phys. Status Solidi* a **110** 189